

Report: Temporal jitter studies at the A0 photoinjector

Timothy Maxwell, Philippe Piot, Jinhao Ruan, Alex Lumpkin, James Santucci
(Dated: May 18, 2009)

Current and upcoming work at the A0 photoinjector requires high temporal beam stability. Recent diagnostics have prompted further study of jitter to identify and isolate sources of any picosecond-level laser/RF timing fluctuations. Streak camera measurements of laser phase are used in conjunction with two different gun phase monitoring techniques to characterize jitter levels and provide an indicator of jitter sources. Basic calibrations and analysis of the statistical accuracy of the various measurements related to the study are also presented.

TECHNIQUE SUMMARY

Previous jitter studies yielded a number of timing fluctuations on varying time scales. As each of the following methods could suggest different sources of jitter, it was decided to run multiple techniques simultaneously and look for any correlations between the different data sets. Some suggested sources of jitter being investigated:

- Master clock (1.3 GHz or downsampled 81.25 MHz)
- Seed laser
- RF gun timing
- The diagnostics equipment

The following are brief descriptions of the various techniques used and what beam components were considered as potential driving sources of jitter. Not mentioned explicitly in these descriptions are the stabilities of the various diagnostic equipment though this can certainly contribute, as will be seen in the analysis.

Throughout this note phase and time of arrival are used somewhat interchangeably, though the author's arbitrary preference is t . These are of course related by

$$t = \frac{\phi}{360^\circ\nu} \quad (1)$$

with ϕ in degrees, ν is the RF frequency in Hz (1.3 GHz for the A0 photoinjector) and t in seconds.

Method A: Laser streak

At the A0 photoinjector, the UV laser reflection from the photocathode window is used to produce a virtual cathode spot for beam positioning on the cathode. An insertable mirror is used to redirect this laser spot from the virtual cathode camera into a Hamamatsu streak camera. After the resulting streak image is phase locked to the system, the centroid of a Gaussian fit to the laser streak in pixels is recorded with a 1 Hz sampling rate. With the appropriate calibration for seconds per pixel, this value is assumed to be the relative time of arrival for the laser pulses to the cathode. Using range 1 for the streak camera, the calibration is given to be 0.32 ps/pixel.

It is assumed that this technique is primarily sensitive to the phase stability of the laser and the streak camera. It should be less sensitive to the stability of the 81.25 MHz master clock as both the laser and streak camera use this as a trigger, excepting the case where there are differing signals in the separate branches from the clock.

Method B: Phase-sensitive charge fluctuation

This technique is referred to throughout as “the charge method.” In this case the sensitivity of the accelerated bunch charge exiting the RF gun to the relative phase between the UV laser and gun's RF is used. As one scans this phase, the bunch charge exiting the gun increases approximately linearly before reaching a $\sim 90^\circ$ -long flattop. From there the surviving charge once again decreases as the emitted electrons begin to be reflected by the gun RF.

Measurement of this phase-charge plot is done by scanning the phase and recording the bunch charge exiting the gun using a calibrated toroidal beam current monitor. In the case that a bunch is comprised of several micropulses, only the charge of the leading bunch in the train is recorded.

Date	Types of data taken			Run Label
	A	B	C	
March 2 nd , 2009	Data	Calibration		B1
		Data	Data	1AB
March 9 th , 2009	Data	Calibration		B2
		Data		3AB
		Calibration	Calibration	B3 C1
March 16 th , 2009	Data		Data	4A
			Calibration	5AC C2
			Calibration	C3

TABLE I: Chronological listing of data sets, which technique was used and which runs were exclusively for calibration purposes. “Run label” is the name given to the respective data set for ease of reference.

To minimize effects due to laser pulse energy variations, a UV energy meter simultaneously records the laser pulse energy associated with each shot. This value is integrated over constituent micropulses in the case where a bunch train is used. This value (divided by the number of pulses in the train) is then used to normalize the emitted charge.

During typical beam operation the phase is set to sit 45° after the start of the rising edge to maximize bunch charge, charge stability and transverse emittance. However, by sitting on the linear rising edge of this phase calibration one may assume that gun charge fluctuations are related to small phase changes between the gun RF and the seed laser. That is we assume the launch phase plot maintains its form but the launch phase $\phi_{Control}$ set on the machine and the actual launch phase ϕ_B may vary. The result is this plot shifting by $\delta\phi_B = \phi_B - \phi_{Control}$. Therefore if one sits on this rising edge and monitors bunch charge, they may resolve gun-laser jitter on the scale of a couple degrees (a few picoseconds). Illustration of this follows in the calibration section.

This measurement is primarily sensitive to the stability of the gun RF phase, laser phase and any discrepancies between the 1.3 GHz master oscillator (gun trigger) and the downsampled 81.25 MHz (laser trigger).

Method C: Beam dispersion

The third and final method relies on the phase sensitivity between the bunch and the 9-cell accelerating cavity. In this setup the gun-laser phase is set to normal operating values and the 9-cell phase is set to deliver the bunch at some off-crest value (25° off crest was used here). The assumption is that phase variations are primarily being driven by gun jitter or drift on the order of a few degrees. In such a case small variations in the cavity-gun phase will translate into small variations in the final energy of the bunch. By then using the dipole spectrometer in the straight ahead we can record shot-to-shot energy fluctuations and relate this back to the incoming phase jitter. Further description for this technique is also elaborated in the calibration section.

Again, this compound process can in principle be driven by a number of timing effects. These include laser timing, gun timing, 9-cell timing and RF stability, and the master oscillator.

Measurement Chronology

Table I summarizes the chronology of the data that was taken, what method of data taking was being used and whether it was for jitter data or calibration of the indicated method. For reference purposes data sets are also given run labels. Here we have numbered calibration runs and jitter data taking runs separately. Runs for calibration are referred to first by the technique being calibrated and second by the number of the data run. Data taking runs are referred to by the number of the data set and then by the letters associated with the data methods that were used.

CALIBRATIONS AND STATISTICAL ERROR

We now look in gross detail at how to correlate the values measured by the various techniques to a corresponding time jitter. In effect these all boil down to simple conversion factors of one form or another dictated by how each method works.

Furthermore we attempt to use statistical data from various calibration runs to get a handle on how timing and measurement noise inherent in the techniques compares to the magnitude of the jitter effect we seek to measure.

Laser Streak (A)

The application of the streak camera yields a relatively direct calibration (provided as 0.32ps/pixel) to relate screen position to laser pulse timing [1]. We have also been given that the accuracy of the streak camera in the best of conditions is limited to 300 fs as determined from the minimum spot size that can be achieved in focus mode.

When comparing this method to the other two presented here there is also an effective jitter compression in the accelerating structures. This stems from the impact of launch phase and RF amplitude jitters on the phase and energy spread of a bunch exiting a cavity [2, 3]. In the case of the present analysis, we would assume that if a jitter measured by the streak camera (before the cathode) is assumed to be a real launch phase fluctuation, that this should be seen in methods B and C (after acceleration) as a reduced jitter.

Therefore we would suggest that if any fluctuations seen in methods B and C are thought to be correlated to the jitter seen in the laser streak (as a presumed launch phase instability), one should take the proper compression factors into account when directly comparing signal amplitudes. This effect is neglected here.

Charge Method (B)

Calibrating this technique requires collecting data on the relationship of the charge exiting the gun versus the laser-gun phase. First, this allows us to determine the location of the linear rising edge of the phase scan where the bunch charge is most sensitive to phase fluctuations. Second, once we start recording charge fluctuations in this range, we require an analytical solution for charge versus phase to map the measured value back to a corresponding time. These are what were determined during calibration runs B1 and B2. It's assumed that this $Q - \phi$ relationship remains relatively fixed for a given experimental setup, only varying by horizontal shifts in phase.

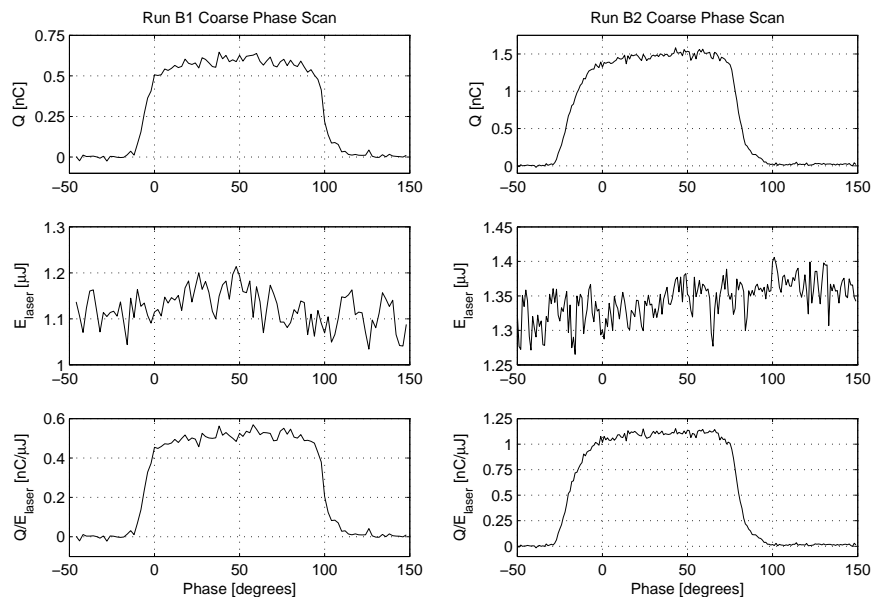


FIG. 1: Coarse laser-to-RF gun phase scans from calibration runs B1 and B2.

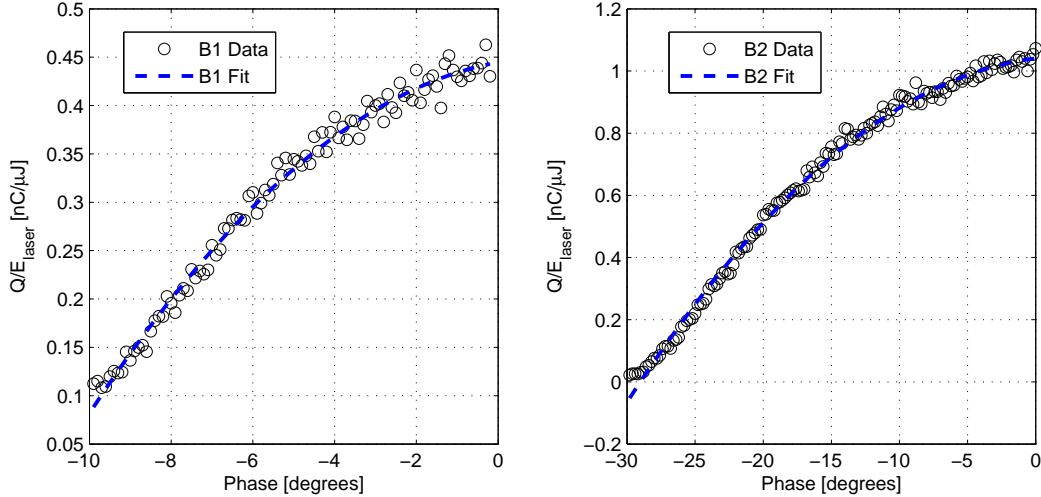


FIG. 2: Fine laser-to-RF gun phase scans from calibration runs B1 and B2 including quadratic fits.

Figure 1 shows the coarse phase scan for both runs. This is used to locate the rising edge. A finer phase scan is then performed over that region. A fit to the fine scan data is then used as the charge-to-time jitter calibration. The resulting scans and fits are shown in figure 2. As the data had noticeable curvature, a quadratic fit was taken instead of linear to allow the fit to more accurately cover a broader phase range.

We use a quadratic fit of the form

$$\hat{Q} = A\phi_B^2 + B\phi_B + C \quad (2)$$

where \hat{Q} is the measured bunch charge normalized to the laser pulse energy in nC/ μ J, and ϕ_B is the gun-laser phase in degrees. Solving for ϕ_B , we find the rising edge calibration for the relative phase in terms of arrival time to be

$$t_B = \frac{1}{360^\circ\nu} \times \frac{\sqrt{4A(\hat{Q} - C) + B^2}}{2A} + t_{B_0} \quad (3)$$

where ν is the RF frequency in Hz, t_{B_0} is some constant reference time with the resulting t_B in seconds. Eq. 3 with the fit coefficients determined in calibration runs are then used to relate values recorded as $\hat{Q}(t)$ during data taking runs back into a relative jitter $\delta t_B(t)$.

Calibration run B3 was performed to get a better estimate of the compound statistical accuracy of this technique. Here we set the launch phase to the center of the flattop. In this case the above calibration does not apply as charge fluctuations have no phase correlation if the launch phase is assumed stable within several degrees. To correlate this to a time jitter we assume the same intrinsic charge fluctuations found in the flattop measurement are still present at any given phase. However, we must then ask if the charge fluctuations recorded in the flattop are strongly correlated to the mean of the recorded charge or if the signal fluctuation is relatively fixed.

First, in the case that the fluctuations are charge dependent, we assume the flattop value relates to the rising edge measurement as a function of the percentage RMS charge fluctuation

$$\epsilon_{\hat{Q},flattop} = \frac{\sigma_{\hat{Q},flattop}}{\bar{\hat{Q}}_{flattop}} \quad (4)$$

and we use eq. 3 to relate it into a time-correlated RMS value as

$$\delta t_{B,stat} = t_B[(1 + \epsilon_{\hat{Q},flattop}) \times \hat{Q}(\phi_0)] - t_B[\hat{Q}(\phi_0)] \quad (5)$$

where ϕ_0 is the laser-gun phase that it's presumed a measurement is oscillating about. This can be either the manually set launch phase $\phi_{Control}$ (set roughly to the center of the rising edge) or, more precisely, the mean of the resulting phases recorded in a data taking run. Where a linear fit is used the phase noise $\delta\phi_{B,stat}$ would simply be $\epsilon_{\hat{Q},flattop}\hat{Q}(\phi_0)$ divided by the slope of the charge versus phase plot.

However, if we assume this jitter does not depend strongly on the mean charge, then we relate the flattop value to the rising edge by simple addition with the estimation

$$\delta t_{B,stat} = t_B[\hat{Q}(\phi_0) + \sigma_{\hat{Q},flattop}] - t_B[\hat{Q}(\phi_0)] \quad (6)$$

Where a linear fit is used $\delta\phi_{B,stat}$ would then be $\sigma_{\hat{Q},flattop}$ divided by the slope of the charge versus phase plot.

Run B3 represents sampling \hat{Q} on the flattop over several minutes yielding $\sigma_{\hat{Q},B3} = 0.028$ nC/ μ J and $\epsilon_{\hat{Q},B3} = 0.024$. The resulting statistical estimate of the corresponding noise levels in data taken using calibrations B1 and B2 are summarized in table II. In the evaluation of t_B needed to compute $\delta t_{B,stat}$ we used $\phi_0 = \phi_{Control}$, the launch phase setting on the control hardware. These phase values are also shown in the table.

The question as to whether the measurement error is charge dependent (equation 5) or independent (equation 6) applies was not considered before the experiment, so conclusive data relevant to the issue has not yet been collected. However, during each of the phase scans there were a small number (2 to 4) data points taken at each phase setting. Also, as can be seen in figures 1 and 2, set up for the runs were such that the ratio of the peak charge in B2 to B1 was ~ 2.5 . Investigation of the rough statistical data available from the phase scans shows both setups having an error on the flattop of ~ 0.03 nC/ μ J despite the noticeable difference in charge. From this we assume that equation 6 more accurately applies to the current discussion.

Incidentally, for the present data, application of equation 6 also yields a looser restriction (larger upper limit) on the intrinsic noise in this method than does 5 as can be seen in table II. So until more precise data is taken, this is our “safe bet” regardless.

Beam Dispersion (C)

The goal in this technique is of course to convert time jitter to an energy jitter, then analyze the energy jitter in a spectrometer (dispersive bend). Working backwards, we first must look at the spectrometer to relate the measured value of viewing plane deflection back to incident energy. As this is the author’s first in-depth look at a spectrometer, he shares his analysis here in gross detail. The basic setup for the spectrometer including hardware as installed at the A0 photoinjector is shown in figure 3. The dipole’s geometry is shown for reference since this is the only physical object on the beamline we have to determine the location of its magnetic field with respect to the beam pipes, screens, etc. Also shown is an associated fringe field for the dipole. This is taken to be a hard-edge model with the field extending a perpendicular distance of 31.4 mm from all edges of the dipole, as determined in the analysis presented in Ref. [4].

The solid curve shown in figure 3 represents the trajectory a particle can follow to the horizontal center of BPM8. Described below, this must follow a circular arc in the field region which terminates smoothly into a linear path at the field’s edge. This curve is characterized by a radius of curvature through the dipole ρ_0 and an ejection angle from the face θ_0 . Given the shape of the dipole, its position with respect to the entering and ejecting beam lines, the extent of its fringe field, and the fixed location of the point we’re trying to hit (the center of BPM8), the values of both ρ_0 and θ_0 have only one unique set of values entirely defined by this geometry.

This is significant in light of the two values most significant for a spectrometer experimentally: ρ_0 and its dependent dispersion value η . When the beam is traversing the center of our viewing plane, taken as (z_{scr}, x_{scr}) in figure 3, we can determine the beam’s mean longitudinal momentum p_0 . The physics dictates that in the dipole’s field region the relationship between the beam momentum p_0 , magnetic field B_0 perpendicular to the page and the fixed radius of curvature of the trajectory to be

$$p_0 = qB_0\rho_0 \quad (7)$$

with q being the elementary charge. So with knowledge of the magnetic field setting B_0 which steers the beam onto the BPM’s horizontal center at (z_{scr}, x_{scr}) and the associated geometric parameter ρ_0 we can find the beam energy.

Run	ϕ_0	δt_{stat} from Eq. 5 [ps]	δt_{stat} from Eq. 6 [ps]
B1	-7°	0.27	1.28
B2	-19°	0.64	1.31

TABLE II: Statistical error intrinsic in the charge method assuming mean charge dependent (Eq. 5) or independent (Eq. 6) measurement errors using $\sigma_{\hat{Q},B3} = 0.028$ nC/ μ J and $\epsilon_{\hat{Q},B3} = 0.024$ from run B3.

One may have an arbitrary path with curvature ρ which still satisfies

$$\rho = \frac{p}{qB} \quad (8)$$

but for some arbitrary momentum p and field B . Assuming one has determined the appropriate ρ_0 and θ_0 , we find the angle of the ejected trajectory to the horizontal θ at the exiting face is a function of arbitrary ρ by

$$\theta = \arcsin \left[\frac{\rho_0}{\rho} \sin(\theta_0 - \alpha) + \left(\frac{\rho_0}{\rho} - 1 \right) \sin \alpha \right] + \alpha \quad (9)$$

where α is the angle between the pole faces. From this we then see that the curve will follow an arc of radius ρ until reaching the point $[\rho \sin \theta, \rho(1 - \cos \theta)]$. From there it will continue in a straight line on a slope defined by $\tan \theta$.

Using this information one can solve exactly for where the exiting trajectory intersects with the viewing plane. If we constrain our region of interest to small variations $(\theta - \theta_0) \ll 1$ and $\rho_0/\rho \ll 1$, we find the horizontal deviation of this ray from the center of the screen (measured along the screen) Δx to first order

$$\Delta x \simeq \eta \frac{\Delta \rho}{\rho_0} \quad (10)$$

where $\Delta \rho = \rho - \rho_0$ and

$$\eta = [\rho_0 + L \tan(\theta_0 - \alpha)](1 - \cos \theta_0) + L \sin \theta_0 \quad (11)$$

is the dispersion coefficient with L as the length of the straight line path from the end of the field edge to the center of the screen. Note that the dispersion η , like ρ_0 and θ_0 , depends solely on the geometry of the experimental setup.

Note that equations 8 and 10 combine to yield the usual dispersion relation

$$\Delta x = \eta \frac{\Delta p}{p_0} \quad (12)$$

Thus η gives us the relation we need for the first part of our calibration. That is: how to convert small deviations in beam energy to deflections seen on the screen and vice versa. All that is left to do is describe how the accelerating cavity is used to convert a small arrival time jitter into an energy jitter to complete the relations.

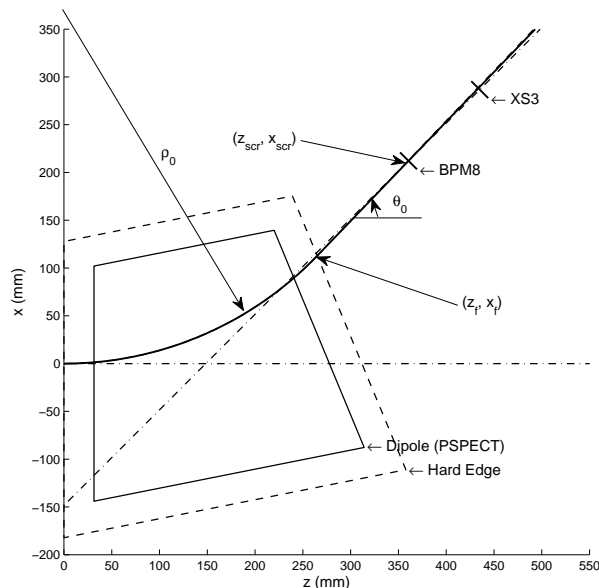


FIG. 3: Geometry of the spectrometer with associated A0 hardware. *Dash-dot* lines are center lines for beam pipes with beam entering from left along $x = 0$. Also drawn is the dipole face (*solid trapezoid*) and an overlaid effective field (*dashed trapezoid*) using a hard-edge fringe field that extends 31.4 mm beyond pole edge as measured in Ref. [4]. The *bold lined* trajectory represents a path centered on BPM8.

However there is still one detail left as we have yet to find the proper values of ρ_0 and θ_0 from the given geometry. Our approach to this problem is offered in Appendix A. A summary of the resulting parameters is presented in table III. We present all values for when the beam is centered on BPM8 versus centering on XS3 and find the difference negligible. These values are also in generally good agreement with values that have been determined previously. It's interesting to note the 1° difference in the ejection angle from the nominal 45° . This would imply that an image centered on one screen would be ~ 2 mm off center on the other if correct.

Assuming we have now found a well-defined dispersion η for our spectrometer, equation 12 lets us relate small changes measured on the viewing plane (BPM8 in our case) to small changes in momentum. To find how these are related to arrival time jitter, we consider the energy gain in the cavity. Given an initial energy from the RF gun of E_{gun} , a maximum (on-crest) energy gain from the cavity E_{cav} and a relative phase ϕ_{cav} between the arriving bunch and RF crest, we have for the energy at the end of the cavity

$$E_{tot} = E_{gun} + E_{cav} \cos \phi_{cav} \quad (13)$$

Consider the case where the arrival phase ϕ_{cav} is not fixed to some set value ϕ_0 , but may contain small fluctuations $\delta\phi_C$ such that

$$\phi_{cav} = \phi_0 + \delta\phi_C \quad (14)$$

For small deviations $\delta\phi_C \ll 1$, we expand E_{tot} about ϕ_0 and find

$$\frac{\Delta E}{E_0} = \frac{-E_{cav} \sin \phi_0}{E_0} \delta\phi_C \quad (15)$$

Where the mean energy E_0 from $E_{tot}(\delta\phi_C = 0)$ is

$$E_0 = E_{gun} + E_{cav} \cos \phi_0 \quad (16)$$

Converting this to relativistic momentum to allow for medium energy beam

$$\frac{\Delta p}{p_0} = \frac{-E_{cav} \sin \phi_0}{\sqrt{(E_{gun} + E_{cav} \cos \phi_0)^2 - E_{rest}^2}} \delta\phi_C \quad (17)$$

Where E_{rest} is the rest energy of an accelerated particle. Finally, combining this with equation 12 and converting phase to time using the RF frequency ν , we have the calibration

$$\delta t_C = \left(\frac{-\sqrt{(E_{gun} + E_{cav} \cos \phi_0)^2 - E_{rest}^2}}{2\pi\nu\eta E_{cav} \sin \phi_0} \right) \Delta x \quad (18)$$

The factor in parentheses therefore allows us to convert deflections from the spectrometer screen's center Δx into a small variation in the time of arrival δt_C .

To find the energy gains from the RF gun and 9-cell cavity we make use of the forward and transmitted power diodes, respectively. Conversions of the values measured on the diodes to the associated peak RF were presented in Ref. [5] which yielded

$$\hat{E}_{cav} = 10.0904 \times [0.0366 V_t + 0.0675 \ln(1 + 18.032 V_t)] \quad (19)$$

$$\hat{E}_{gun} = 26.636 \times [0.0196 V_f + 0.0446 \ln(1 + 3.642 V_f)] \quad (20)$$

with the values \hat{E} in MeV/m and power forward V_f and power transmitted V_t diode readings in mV.

Target	ρ_0 [mm]	θ_0 [deg]	η_{bpm8} [mm]	η_{xs3} [mm]
BPM8	368	46.1	231	322
XS3	370	45.8	229	319

TABLE III: Primary trajectory parameters ρ_0 and θ_0 found analytically for A0 dispersive bend (PSPECT) geometry listed for centering on BPM8 or XS3 with associated dispersions η .

Further converting the peak field value to total energy gain through each element requires further simulation/integration. This calculation for the 9-cell is carried out in the appendices of [5]. We have also performed a similar scan of resulting gun energy versus the gun's peak field using ASTRA (no space charge) for peak fields in the range of 20 MeV/m - 40 MeV/m with the gun's launch phase on the flattop (45° from zero crossing) The conversions to energy gains E in MeV are then

$$E_{cav} = 0.5176 \hat{E}_{cav} \quad (21)$$

$$E_{gun} = -(3.607 \times 10^{-4}) \hat{E}_{gun}^2 + 0.1478 \hat{E}_{gun} - 0.8377 \quad (22)$$

For our runs, the typical diode readings $V_t = 52.1$ mV and $V_f = 51.4$ mV yield peak gains of $E_{cav} = 12.4$ MeV and $E_{gun} = 3.6$ MeV. This was consistent with the spectrometer reading of $E_0 = 16.0$ MeV when running the TESLA cavity on crest.

In conversion equation 18 we determined the necessary η by geometric considerations. There is another way to perform this calibration using small changes in the dipole current. This measurement was also carried out but requires making assumptions regarding the current to magnetic field relationship. It was found, however, that hysteresis effects when making only small changes to the current yielded largely differing values of η . As a matter of completeness and to be sure no data is left behind, some discussion on this is carried out in Appendix B.

In setting up for the jitter measurement described here, a gun phase scan is performed and the launch phase is set to 45° from the zero crossing of the scan to run at the center of the flattop. The 9-cell TESLA cavity phase is then scanned using the spectrometer to find the minimum energy spread corresponding to on-crest acceleration. This on-crest phase setting was used in all of our calibration runs. To introduce the above timing-energy correlation, the set point on the phase was shifted to 25° off-crest ($\phi_0 = -25^\circ$) for data taking runs.

While the calibration sets C1, C2 and C3 were intended to carry out the experimental determination of η explained in Appendix B, they were also used in the estimation of statistical error associated with this jitter measurement. Similar to the error analysis for method B, we assume that when running on-crest that we aren't sensitive to any RF gun-to-cavity jitter. Indeed, with $\phi_0 = 0$, we see from equation 18 that it would take a jitter δt_C exceeding first order to cause a deflection seen on the screen as Δx .

Then by running on-crest we intend to see what other fluctuations are inherent in the beam line. Again assuming that these are present independently of what phase we are running, the measured RMS value of $\Delta x_{rms}(\phi_0 = 0)$ is scaled by the conversion factor in equation 18 using the value of ϕ_0 associated with that data run. This then provides our estimate of some error bar $\delta t_{C,stat}$ that sums in quadrature to the jitter measurement.

For the following data taking runs which made use of BPM8 as the viewing screen, we find the calibration to be:

$$\delta t_C \simeq \left[1.52 \frac{\text{ps}}{\text{mm}} \right] \Delta x_{bpm} \quad (23)$$

accurate to a few percent despite slight differences in beam energy for the different runs. Using the statistical $\Delta x_{rms}(\phi_0 = 0) = 0.215$ mm, we estimate

$$\delta t_{C,stat} \simeq 325 \text{ fs} \quad (24)$$

JITTER DATA AND ANALYSIS

Using the calibrations detailed in the previous sections, we now present the timing fluctuation data listed in table I. To facilitate the comparative studies, there were a few final analyses applied.

Laser streak jump removal

One timing issue previously surfaced when ~ 9 ps discrete jumps were found in data recorded using the streak camera. As we sought to determine whether or not this was isolated to an issue with the streak camera (which was ultimately the case), these jumps were removed from the raw data for comparison to the other methods to verify that the data was otherwise correlated.

This algorithmic data "fixing" is shown for the streak data from run 1AB in figure 4. The points below some arbitrary threshold line (shown as the dashed line in figure 4) are removed from the set which is necessary for cleanly

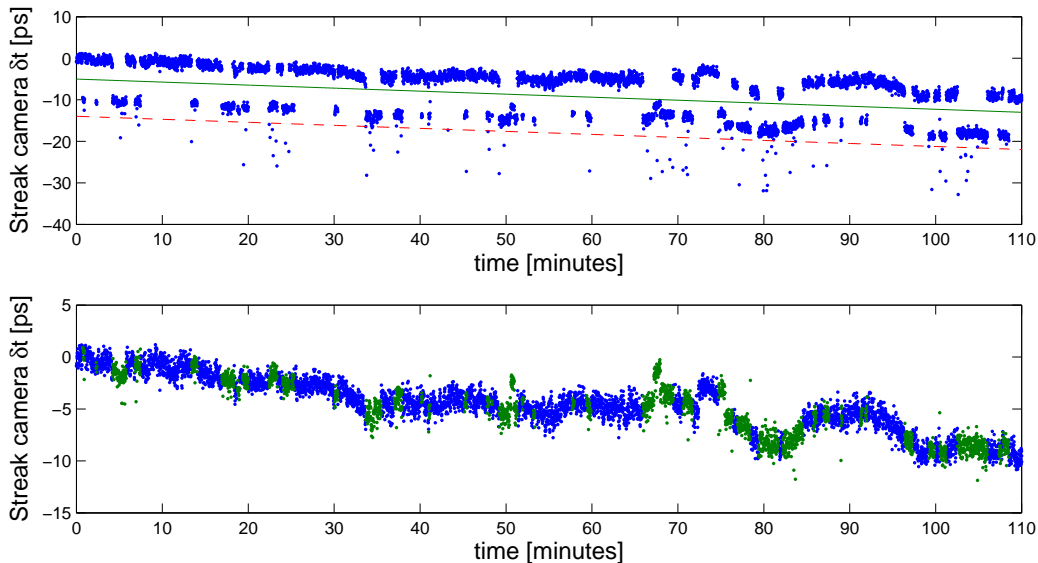


FIG. 4: (Color) Streak data from run 1AB before (*top*) and after (*bottom*) applying removal of 9.4 ps discrete jumps with data snapping technique. Points below dashed line are ignored. Remaining points below solid line are “snapped” to neighboring data points. These blocks are shown in green on bottom figure.

performing the next step. The data is scanned and blocks of data where the values drop below some second arbitrary line (shown as the solid line in figure 4) are identified as a data jump. For each block we calculate a data snap as

$$\text{Snap} = \text{Mean}(\text{Last 10 unsnapped}) - \text{Mean}(\text{First 10 of block}) \quad (25)$$

The snap value is then added to each data point in its associated block, shifting each block systematically back up to the rest of the data. The result is a relatively well connected set of data.

As we shall see, the fixed data sets otherwise showed apparent correlation to data taken with other methods. With this additional motivation it was discovered that the reference signal to the phase lock loop on the streak camera was too strong for “range 1,” the finest scan range. By attenuating the input the jumps were eliminated in data taken using range 1 of the streak camera.

Comparative statistics used

While the high-frequency component of the recorded data will offer a look at shot-to-shot jitter, long-period correlations of the data becomes difficult. In an effort to quantify the comparison of the simultaneous data sets some smoothing and statistics have been applied.

To start, we apply a flat moving average to each set to smooth out the high frequency jitter in the signals for each set. This improves qualitative comparisons of longer drifts in the signals.

Two plots are then offered to investigate correlation. The first is a scatter plot of one smoothed data set against the other. From this we look for linearity between the full data sets.

We then look for local correlations by plotting moving R^2 values. These are computed using data taken from subsamples of the smoothed data sets over the range $(t - \Delta t/2, t + \Delta t/2)$, where Δt is some stated data window. For some associated data subsamples X and Y , we use

$$R = \frac{\text{Cov}(X, Y)}{\sigma_X \sigma_Y} \quad (26)$$

In effect this number indicates the goodness of fit of the stated data block X to the associated data window Y from the the other data. This offers a strong indication of correlation as a function of time in a single plot, though one now might ask the question of what an appropriate time window would be.

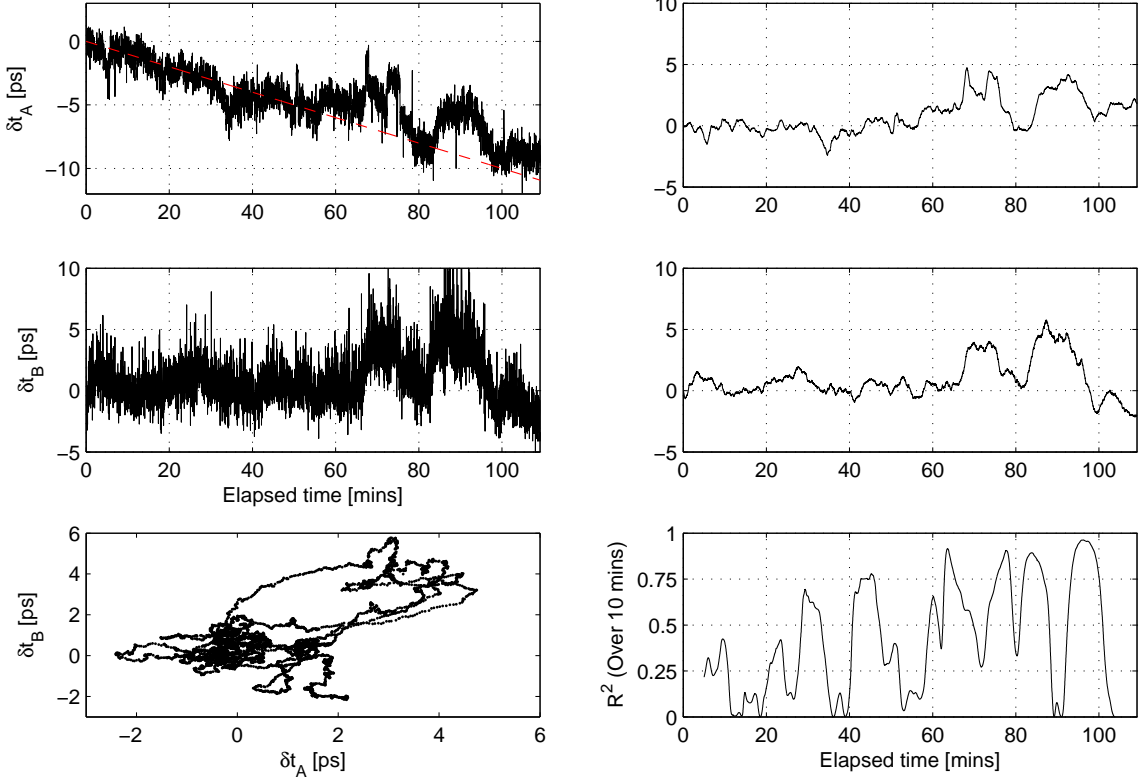


FIG. 5: Raw data from run **1AB** (*top two, left*) with smoothed moving averages (*top two, right*), 10 minute moving correlation of smoothed data (*bottom-right*) and smoothed data scatter plot (*bottom-left*). The smoothed data for method A has also had 0.1 ps/minute [dashed line (*top-right*)] removed.

Indeed, application of these sorts of statistics is somewhat arbitrary. For the moving averages we’ve tried to only smooth as much as would remove high-frequency components without washing out any distinctly “real” sharp peaks in the data. Our choice of a correlation data window width Δt used in the moving R^2 value is somewhat less arbitrary as this value sets the time scale of features we are comparing. We’ve selected the correlation windows to compare roughly to the length of long term drifts and bumps in the given data which varied on operating conditions.

From these we seek what one might consider sufficient correlation, though the definition of “sufficient” is a judgement call. Where agreement is good we assume that the timing fluctuation in that range has a shared cause.

Run 1AB

This first data taking run compared timing information using the laser streak method (A) to that of the charge technique (B). The raw data, smoothed data, and correlation plots are shown in figure 5. As noted previously, ~ 9 ps jumps have been removed from the raw streak data.

Furthermore we note a running drift of ~ 100 fs/min in the raw streak data that was removed in generating the smoothed plot on the right. The justification for this is in a warmup time known to be associated to the streak camera. The usual operating procedure is to warmup the camera for about twenty minutes before operating as it otherwise loses its phase lock. However, as seen here, a drift is still noticeable after this warmup and, if one is to believe the charge method data, seems to flatten out somewhere in the 60 - 80 minute range.

Analysis of the raw data in the relatively flat region over the first hour yields an RMS jitter of 0.5 - 1.0 ps by the laser streak method and 1.0 - 1.5 ps via charge method, both values on the order of associated measurement noise. However, the behavior begins to be dominated by the drifts seen in the smoothed trace.

Both appear to contain relatively quiet drifts of about 2.5 ps (min-to-max) initially. These expand to a pair of

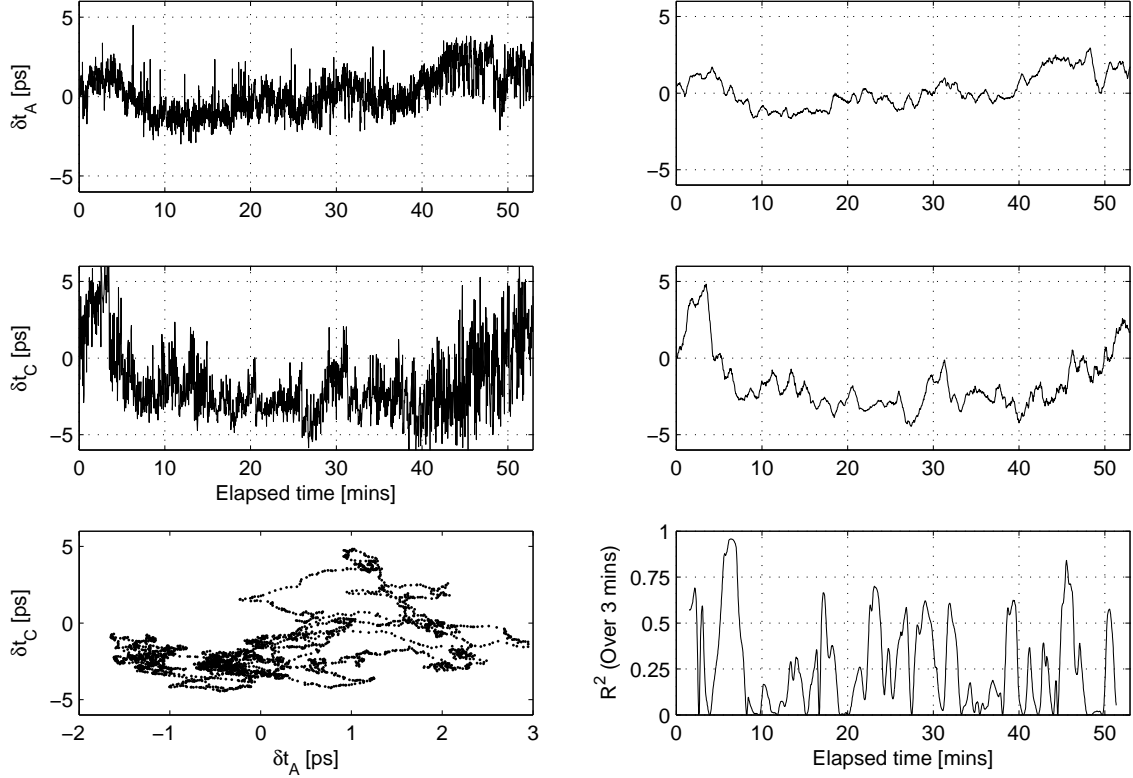


FIG. 6: Raw data from run **2AC** (*top two, left*) with smoothed moving averages (*top two, right*), 3 minute moving correlation of smoothed data (*bottom-right*) and smoothed data scatter plot (*bottom-left*).

larger bumps toward the second hour seen as large 6 ps drifts over 15 minutes. The rippling appears in the scatter plot as two relatively uncorrelated clusters connected by four somewhat linear curves. The clusters themselves are associated with the noisy peak and valley values of the plots and appear macroscopically correlated. The R^2 plot identifies four regions with better than 80% correlation that are associated directly with the rising and falling edges of these bumps that connect the clusters of the scatter plot.

From this we associated these long 6 ps drifts to equipment shared by both techniques being used. In our setup this implicates some element in the laser line between and including its individual leg of the subsampled 81.25 MHz master clock to the RF gun.

Run 2AC

The data for this run using the laser streak (A) and spectrometer (C) is shown in figure 7, with laser streak data repaired again by the snapping algorithm. This run was started about an hour after run 1AB. RMS jitter levels over the quietest 15 - 25 minute region is again in the range of 0.5 - 1.0 ps for both data sets.

Correlation of these data sets isn't quite as clear. They seem to correspond well in the first several minutes. The drift of the means was ~ 4 ps and ~ 8 ps over about 5 minutes for sets A and C, respectively. Both data sets also show increased high frequency noise levels in the last twenty minutes though these are again much more pronounced in the spectrometer measurement. In set A the RMS noise level increased to 0.8 - 1.5 ps, and for set C to 2.0 - 3.0 ps.

For these data sets it's difficult to justify the perceived dependence of the spectrometer data on that seen by the streak camera. It may be that additional effects downstream of the cathode dominated timing fluctuations for this data run which may also be contributing to difference in scale. The difference in scale may also be due in part to compounded timing compression effects through the RF gun and 9-cell cavity. Overall we consider these data more

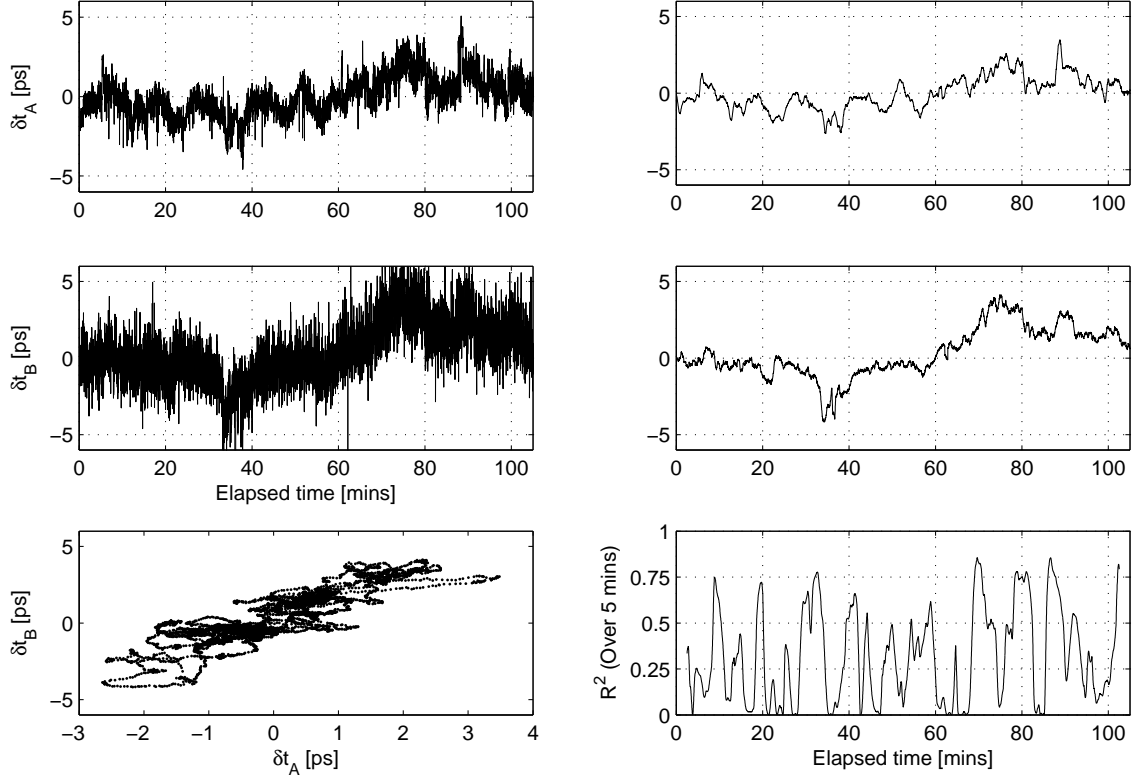


FIG. 7: Raw data from run **3AB** (*top two, left*) with smoothed moving averages (*top two, right*), 5 minute moving correlation of smoothed data (*bottom-right*) and smoothed data scatter plot (*bottom-left*).

or less uncorrelated and that the differences are due mostly to unstable 9-cell behavior, though the numbers still offer some insight into behavior before and after the cavity.

Run 3AB

Snapped laser streak (A) and charge method (B) data for run 3AB are shown in figure 7. Over regions of small drift, RMS noise levels are again in the ranges of 0.5 - 1.0 ps for method A and 1.0 - 1.5 ps for method B.

The scatter plot shows a broad linear grouping. This is seen in the smoothed data first as a number of short, weakly correlated drifts. For both sets these are on the order of the high frequency jitter at about 1 - 2 ps or less over a few minutes.

The long ramp from 35 - 75 minutes appears correlated at the initial valley and the final crest. This measures 5 ps min-to-max on the streak data and 8 ps on the charge technique.

Overall the system seemed relatively quiet for this data run by either measurement within the noise limits of these diagnostics. Furthermore, this data pair is considered relatively well-correlated for the weak signal drifts observed. This suggests what small jitter was seen was again primarily driven by the seed laser.

We also note that the seed laser was given an overnight warmup before starting this run which seems to have helped minimize large amplitude, short (few minute) duration “bumps” considerably. The following two runs were performed in an effort to observe more erratic seed laser behavior.

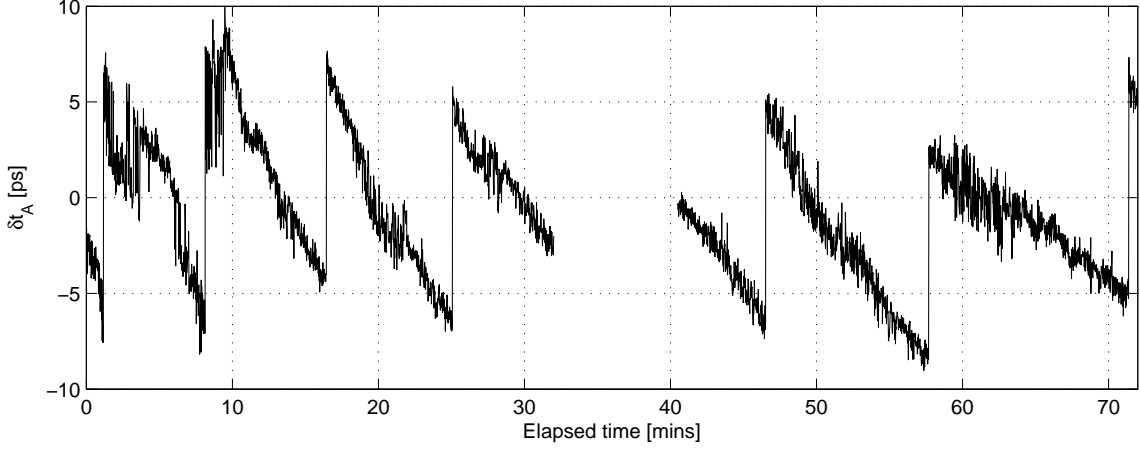


FIG. 8: Raw laser streak data from run 4A.

Run 4A

For this run we intentionally targeted laser timing fluctuations driven by running the laser after only a few hours of warmup. As we set up for the spectrometer measurement we immediately started recording laser streak data which is shown in figure 8. The gap in the data from 33 - 40 minutes was due to a briefly unnoticed loss of phase lock on the streak camera.

Note that this data set required no snapping algorithm as the discrete, square jumps were not observed. Again, the issue with the streak data was found between this and the prior run to be due to high trigger input levels to the streak camera's phase lock loop circuit. After adding a 3 dB attenuator the jumps disappeared on the fine range 1 scans.

Yet again the high-frequency component of the jitter registers at 0.5 - 1.0 ps. We now observe a very strong sawtoothed pattern to the drift, as was expected. In this run it was suspected that running the laser cold would result in this effect as the cavity and CLX (phase lock system) of the laser heat up. Starting cold the system must continually move a compensating mirror via piezo motor in an attempt to keep up with the thermal drift. This is seen as the long, negative slope. This continues until reaching the limit of travel. At this point a stage motor shifts the mirror a larger step which causes the large timing jump.

For this data it appears that the magnitude of the jumps are consistently 15 ps, excepting the last full drift cycle. Note that over time the duration of the drifts between jumps increases steadily. The first drift lasts 7.0 minutes while the last complete observed drift lasts 13.5 minutes. This trend of longer drift cycles continues into the following run 5AC which was started within minutes of the end of this run's conclusion.

Run 5AC

The final run of the raw laser streak (A) and spectrometer method (C) data are shown in figure 9. We begin by noting the best high-frequency noise levels which appear in both data sets in the neighborhood of 20 and 45 minutes. At these points the RMS jitter levels were a relatively stable 0.5 ps for streak set A and 0.5 - 1.0 ps for spectrometer set C.

Next note the very strong correlation observed on the common sawtooth features of both sets. Where high-frequency noise was small, this pattern is distinct in both the streak and spectrometer. This is also seen in the highly linear scatter plot for $\delta t_A > 1$ ps and $\delta t_C > 2$ ps, matching with the smoother upper halves of both plots. From this we corroborate that the large, distinct sawtooth timing fluctuation is due to cold laser operation.

For the mean streak data we saw a 6.7 ps drift over 26.5 minutes for the first complete cycle and 11.5 ps over the last 30 minutes. On the spectrometer this appeared as a 4 ps drift and an estimated 10 ps.

An interesting feature of this comparison is the change in the high frequency noise level at certain times. Most striking is over the last twenty minutes where the apparent jitter at the spectrometer increased. This was clearly not due to laser timing instability as the noise levels measured at the streak camera remained relatively fixed. As the

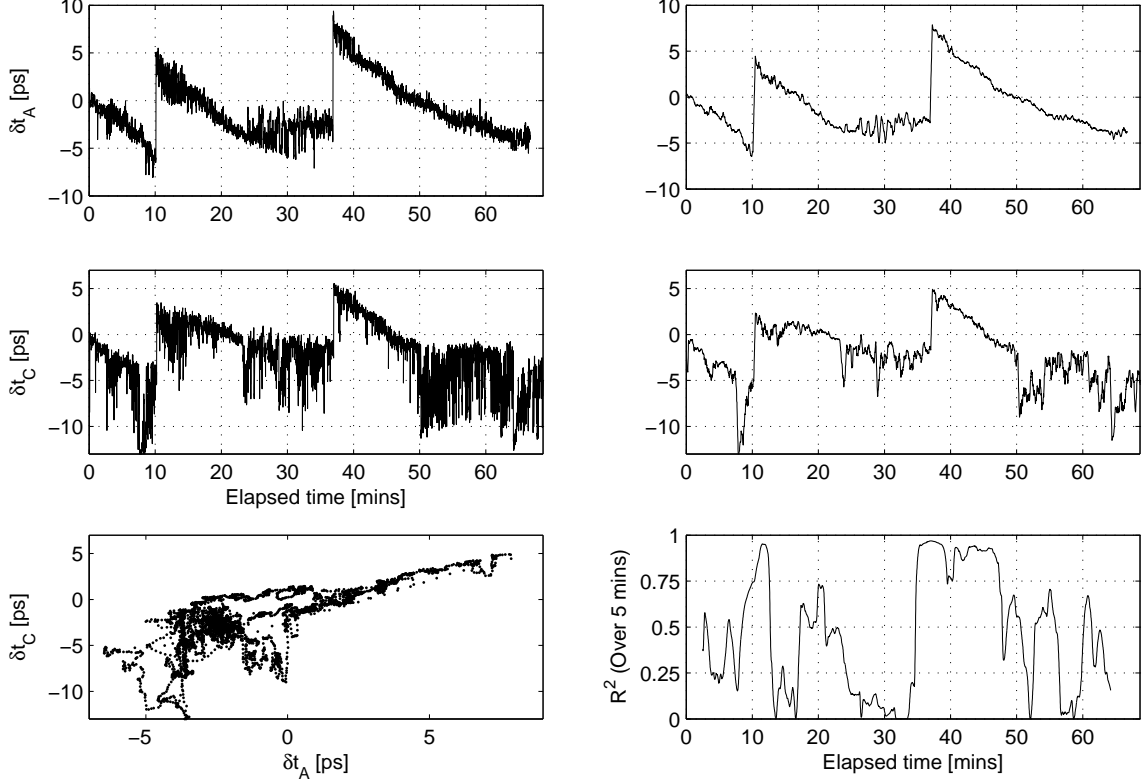


FIG. 9: Raw data from run **5AC** (*top two, left*) with smoothed moving averages (*top two, right*), 5 minute moving correlation of smoothed data (*bottom-right*) and smoothed data scatter plot (*bottom-left*).

spectrometer measurement is actually an energy jitter measurement (though it's certainly sensitive to a number of timing issues), we must presume this was due to some problem in the RF gun or 9-cell stabilities. The 9-cell cryo system was checked and appeared stable at the time of this noise spike.

Over the time periods from 10 - 15 minutes and 22 - 40 minutes, however, noise levels for both measurements increased simultaneously. For the first range this was 1.0 - 1.5 ps on set A and 1.0 - 3.0 ps for set C. In the second time range it was 1.0 - 1.8 ps for set A and again 1.0 - 3.0 ps for set C. With this being a high-frequency effect on data collected at 1 Hz, correlation is difficult to determine by direct analysis. We also don't have the extended discussion on timing compression effects in the cavities alluded to earlier to explain matters of scale. But given the coincidental durations a connection seems plausible.

SUMMARY AND CONCLUSIONS

Three methods for the measurement of timing fluctuations have been presented and applied to operations at the A0 photoinjector. A number of battling factors have been resolved as a result.

Previous findings of the 9 ps discrete jumps in streak data have been resolved. The attenuation of the reference signal has allowed for clean operation of the camera at its finest scale. We also noted in the first run 1AB a running 0.1 ps per minute slope over the first hour of streak measurements not present in the compared method. This was a known effect of streak warmup. We might suggest that an automated or remote early startup for the streak camera be implemented to improve streak accuracy at the start of the day.

In studying the laser as a driving factor the overall system jitter, 0.5 ps was observed as the best operating value by the streak method and 1.0 ps by the other techniques. At these levels we extend beyond the limits of the diagnostics themselves.

The large sawtooth drift was also verified to be due to cold laser operation, as was already understood. However, in data sets where the system was well prepared, drifts exceeding 2 ps were observed by all methods that seemed to stem from the seed laser system. The longer time scale of these smaller drifts may be difficult to compensate for. The ultimate limit to any corrections would depend on the time resolution of the seed laser's CLX system. Such a solution to laser phase drifts greater than a picosecond are currently being pursued.

Much of this analysis was driven by the question of how significantly the seed laser was driving timing issues. Some question regarding the differences in scale of the various methods may help further extend the use of the data collected. An estimate of the statistical error of the methods was presented, yielding 1.2 ps for the charge technique and a likely low estimate of 300 fs using the spectrometer. By more carefully investigating timing propagation down the beamline coupled with the data collected for this report, more explicit contributions to final beam jitter by other hardware may be found.

-
- [1] A. H. Lumpkin and J. Ruan (2008), presented at 13th Beam Instrumentation Workshop (BIW08), Lake Tahoe, California, 4-8 May 2008.
- [2] P. R.-G. Piot, "Analysis of beam-based measurement of absolute phase jitter between an accelerating structure and a relativistic electron bunch", FNAL Beams Doc, 3335-v1, <http://beamdocs.fnal.gov/DocDB/0033/003335/001/jitter.pdf> (March 2009).
- [3] P. Piot, R. Tikhoplav, D. Mihalcea, and N. Barov, Phys. Rev. ST Accel. Beams **9** (2006).
- [4] K. Bischofberger, "FNPL spectrometer recalibration", unpublished work available at <http://nicadd.niu.edu/fnpl/docs/kip-spectrometer.pdf> (August 2002).
- [5] P. R.-G. Piot, "Notes on beam energy measurements at FNPL", FNAL Beams Doc, 1132-v1, http://beamdocs.fnal.gov/DocDB/0011/001132/001/energy_note.pdf (April 2004).

APPENDIX A: SPECTROMETER CALIBRATION BY GEOMETRY

To begin we offer the constraints on the geometry dictated by the setup.

Referring back to figure 3, the origin of our system is located at the point where the beam enters the dipole's magnetic field. As previously stated, from here it must follow a circular arc until the arc intersects the line that defines the end of the dipole field under the hard edge approximation. Given the proper parameters for the dipole geometry and placement with respect to the straight-ahead line, the field's termination line is completely defined. To be clear, this is to say that the point (z_f, x_f) shown in figure 3 is constrained to a terminating line $x(z)$.

Further, that the particle is assumed to enter traveling in the z direction along $x = 0$ and be constrained on the arc in the field region, we have that

$$\begin{pmatrix} z_f \\ x_f \end{pmatrix} = \begin{pmatrix} \rho_0 \sin \theta_0 \\ \rho_0(1 - \cos \theta_0) \end{pmatrix} \quad (27)$$

The final constraint is that we want the ejection angle from the dipole to be such that the subsequent linear trajectory hits the point (z_{scr}, x_{scr}) . In figure 3 we've taken this to be the center of BPM8. This constraint can be written as matching the slopes of the arc and line of our piece-wise function at the end of the field as

$$\tan \theta_0 = \frac{x_{scr} - x_f}{z_{scr} - z_f} \quad (28)$$

These constraints are sufficient to uniquely determine the value of ρ_0 and its associated ejection angle θ_0 that yields the only physically allowed trajectory to the center of our screen at (z_{scr}, x_{scr}) . The author's (perhaps inelegant) solution involved finding the value of z_f that met the constraints. This required a reduction of a cubic equation in z_f . The inputs to define the necessary geometry were taken to be those readily taken from reference points in the lab as

- Bases (192.2 mm, 288.3 mm) and height (241.3 mm) defining the trapezoidal dipole face
- The center of the entering beam pipe to the bottom, left corner (see figure 3) of the dipole tip (144 mm)
- The center of the ejecting beam pipe to the bottom, right corner (see figure 3) of the dipole tip measured along the dipole's edge (194 mm)

- Center of BPM8 and XS3 to pole tip surface measured along exiting beam line (170.6 mm and 276.1 mm, respectively)
- Angle of ejected line to straight-ahead line (assumed to be 45°)
- Additional fringe field width (31.4 mm from [4])

With the exception of the additional fringe field width, all other values were taken from the machine drawings for the beam line. As “things change,” they were also measured as best as could be by hand in the laboratory to verify nothing had been moved. The agreement was sufficient. A MATLAB code was written to accept the above geometry and determine the ρ_0 and θ_0 for beam centering at different positions down stream on the deflected beam line.

Now having solutions for these characteristic parameters we can evaluate the dispersion at our viewing planes using equation 11. It’s worthwhile noting that L called for in 11 is the length of the ray from the end of the field to the center of the screen. It may be more convenient to use the distance L' measured from the center of the screen to the edge of the dipole’s face. To do so we account for the extent of the fringe field by evaluating L as

$$L = \frac{L' \cos(\theta_{pipe} - \alpha) - d_{fringe}}{\cos(\theta_0 - \alpha)} \simeq L' - \frac{d_{fringe}}{\cos(\theta_{pipe} - \alpha)} \quad (29)$$

with θ_{pipe} being the angle between the straight-ahead and ejecting beam pipes, α the angle between the pole faces and d_{fringe} being the distance the faux hard edge extends beyond the edge of the pole tip.

The previously mentioned MATLAB code was later expanded to simulate and draw the trajectories of multiple particles of varying energies for a fixed magnetic field and vice versa. The output of these are the positions on the viewing screens of the various different rays. As a “sanity check,” simulations using multiple particles spaced over a small energy spread ΔE about some primary energy E_0 were performed. Taking the slope of the resulting Δx versus $\Delta E/E_0$ plot yielded dispersions η (see equation 12) in excellent agreement with those calculated in table III.

APPENDIX B: DISPERSION CALIBRATION BY DIPOLE CURRENT AND HYSTERESIS

Here we investigate how to determine the dispersion η of the spectrometer using small variations in current as well as how magnetic hysteresis may have frustrated our attempt to do so.

As the dispersion relates to small fluctuations about the screen center, it is assumed that one begins experimentally by targeting the beam appropriately. When this is satisfied we know that relation 7 is satisfied so that, depending on the mean longitudinal beam momentum p_0 , the value of B_0 is fixed by the value of ρ_0 associated with the screen being used.

Using equation 8 with a fixed momentum p_0 , we instead vary B and evaluate the $\Delta\rho/\rho_0$ of equation 10 to find the dispersion relation

$$\Delta x = -\eta \frac{\Delta B}{B} = -\eta \frac{\Delta I}{I} \quad (30)$$

where I is the dipole current in the case of a well-behaved solenoid satisfying $B(I) = \alpha I$ with α being some constant.

From this we see that by making small variations ΔI in the solenoid current, recording the small deflection from screen center Δx and plotting $\Delta x(\Delta I/I)$, the slope of this curve will yield the dispersion η . This of course assumes a stable beam energy over the duration of the measurement.

Calibration runs C1 - C3 were an attempt to perform this measurement. However runs C1 and C2 yielded dispersions ($\eta_{bpm8} \simeq 180$ mm, $\eta_{xs3} = 257$ mm) in large disagreement with the values predicted from the predictions based on the geometry ($\eta_{bpm8} = 230$ mm, $\eta_{xs3} = 320$ mm). It was suggested by Tim Koeth that hysteresis affects these numbers and that one should always begin by varying the spectrometer current back and forth from -11A to +11A a few times and take data only when coming back up from -11A. This was done before repeating the calibration in run C3 and yielded much closer values of $\eta_{bpm8} = 228$ mm and $\eta_{xs3} = 328$ mm.

Previous analysis of the dipole hysteresis curve in [4] seemed to predict that magnetization should not have had such a significant effect. I would suggest that the hysteresis is behaving differently for these small current variations (~ 50 mA) than would occur for large variations ($\sim 1A$). Assuming this may be the case, we attempt to quantify the effect seen in the experiment.

To begin, let’s compare the ideal field-current relationship $B_{No-Hys}(I)$ to the field $B_{Hys}(I)$ which we take as the first order expansion of the hysteresis curve about the point $I = I_{0,Hys}$. We don’t know the hysteresis in principle, but we

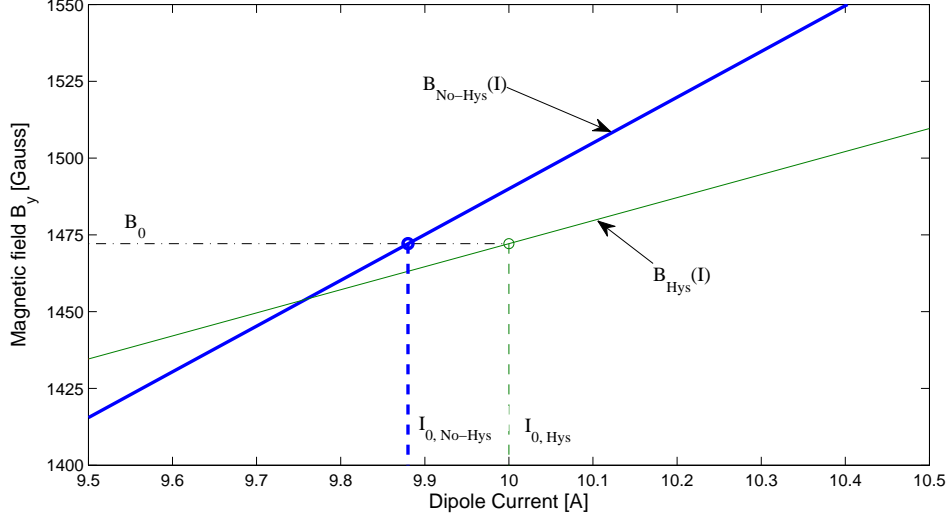


FIG. 10: Illustration of magnetic field curves with and without hysteresis effects in the neighborhood of the field value B_0 that centers the beam on the spectrometer screen.

can estimate what it was using values measured during calibration attempts. These curves can be written

$$B_{\text{No-Hys}}(I) = B'_{\text{No-Hys}} I \quad (31)$$

$$B_{\text{Hys}}(I) = B_0 + B'_{\text{Hys}}(I - I_{0,\text{Hys}}) \quad (32)$$

where the values B' are the slope of the respective curves. We find it convenient to expand $B_{\text{Hys}}(I)$ about the value of $I_{0,\text{Hys}}$ that centers the beam on the viewing screen. This is the point we operate around experimentally and we assume the value of B_0 can be determined by knowledge of ρ_0 and the beam energy taken by some other means. The correspondence between the curves is illustrated in figure 10. Evaluation of the different effective values of η that would be determined for these relations via equation 10 yields the relationship

$$B'_{\text{Hys}} = \frac{\eta_{\text{Hys}}}{\eta_{\text{No-Hys}}} B'_{\text{No-Hys}} \quad (33)$$

Taking $B_{\text{No-Hys}}$ to be the calibration taken in [5] in terms of the current read out by the control system, we would have $B'_{\text{No-Hys}} = 149.32 \text{ Gs/A}$. We compute B_0 based on the beam energy taken from the diode readings for the various runs to get the corresponding value of $I_{0,\text{No-Hys}}$ that would center the beam. For $I_{0,\text{Hys}}$ we use the point where the $\Delta x(I)$ data fit crosses $\Delta x = 0$. Finally, using the values of η as determined above, we estimate the current-field curves from the calibration runs to have been:

$$B_{C1}[\text{Gs}] \simeq 117 \times I_{C1}[\text{A}] + 298 \quad (34a)$$

$$B_{C2}[\text{Gs}] \simeq 113 \times I_{C2}[\text{A}] + 335 \quad (34b)$$

$$B_{C3}[\text{Gs}] \simeq 148 \times I_{C3}[\text{A}] - 17 \quad (34c)$$

It's also worthwhile to note that the centering currents $I_{0,\text{Hys}}$ were approximately equal to the values $I_{0,\text{No-Hys}}$ within about 1%. So the larger current scan and associated current-to-field calibration to find the beam's mean momentum appears to still be consistent with the values predicted by the diodes. Furthermore this implies that contributions to the effective remnant terms in equations 34 are being driven entirely by the different pseudo-dispersions measured over small current variations.

In the neighborhood of the operating current, we see larger remnant fields from an apparent reduced dispersion as measured under the assumption of no remnants. Whatever the cause, it's clear that small relaxations of the applied field after a long-applied positive field yield a different local hysteresis than previously demonstrated in [4].

There's been discussion about returning to an investigation of the spectrometer hysteresis. From these results it's clear that the standard degaussing routine is critical and we would otherwise expect behavior to then be repeatable

under a variety of conditions. Ideally the installation of a permanent Hall probe on the PSPECT chromatic bend at A0 for the precise measurement of the field would still be the best long-term solution. But we would suggest that a more detailed analysis of the hysteresis will not be necessary at this time so long as the dipole continues to be degaussed as a matter of procedure.